Leng *et al. Chem Synth* 2024;4:20
DOI: 10.20517/cs.2023.64

Chemical Synthesis

Research Article

Open Access

Macrocycle-based covalent-organic-polymer as efficient oxygen electrocatalysts for zinc-air flow batteries

Yiming Leng, Tengge Chen, Yuanyuan Yin, Jizhen Li, Xueli Li*, Zhonghua Xiang*

State Key Laboratory of Organic-Inorganic Composites, Beijing University of Chemical Technology, Beijing 100029, China.

***Correspondence to:** Dr. Xueli Li, Prof. Zhonghua Xiang, State Key Laboratory of Organic-Inorganic Composites, Beijing University of Chemical Technology, 15 East North Third Ring Road, Beijing 100029, China. E-mail: m18810868361@163.com; xiangzh@mail.buct.edu.cn

How to cite this article: Leng Y, Chen T, Yin Y, Li J, Li X, Xiang Z. Macrocycle-based covalent-organic-polymer as efficient oxygen electrocatalysts for zinc-air flow batteries. *Chem Synth* 2024;4:20. https://dx.doi.org/10.20517/cs.2023.64

Received: 16 Dec 2023 **First Decision:** 31 Jan 2024 **Revised:** 26 Feb 2024 **Accepted:** 7 Mar 2024 **Published:** 3 Apr 2024

Academic Editor: Xiang-Dong Yao **Copy Editor:** Dong-Li Li **Production Editor:** Dong-Li Li

Abstract

Covalent organic polymers (COPs), as emerging porous materials with well-defined architectures and high hydrothermal stability, have attracted extensive attention in the field of electrocatalysis. Herein, we report a rational design method for preparing oxygen reduction reaction electrocatalysts with the assistance of a predesigned macrocyclic COP model molecular. With the predesigned nitrogen position and structural features in macrocyclic chain-like COP-based materials, the obtained COP_{MCT}-Co-900 catalyst provided excellent oxygen reduction performance, where the half-wave potential ($E_{1/2}$) reaches 0.85 V (*vs.* RHE), comparable to commercial Pt/C. We also extended the strategy to similar macrocycle COPs and Fe-based and Ni-based metal sources and studied the oxygen reduction reaction performance of corresponding catalysts, proving the universality of the method. Interestingly, we assemble COP_{MCT}-Co-900 catalyst as air electrode catalyst of the self-made rechargeable zinc-air flow batteries, which exhibit outstanding power density (155.6 $mW \cdot cm^{-2}$) and long cycle life (90 h, 270 cycles at 10 $mA \cdot cm^{-2}$). Our studies provide a new method for the development of high-performance oxygen electrodes applied in zinc-air flow battery devices.

Keywords: Oxygen reduction, covalent organic polymers, electrocatalyst, zinc-air flow batteries

INTRODUCTION

Over the last decades, efficient design and research of non-precious metal catalysts (NPMC) have made significant progress in oxygen reduction reaction (ORR) electrocatalytic activity and stability[1-6]. The current NPMC systems mainly include transition metal (TM) nitrogen-doped carbon[7-13], supported TM oxides[14,15], TM carbides[16-18], heteroatom-doped carbon materials, *etc*.[19-21]. Among them, macrocyclic compounds have received widespread attention due to their unique 2D topology structure, high conjugation, and redox-rich chemical properties, exhibiting great potential to replace platinum-based catalysts[22-24]. Macrocyclic compounds are composed of various ligands, such as tetraazamacrocyclic porphyrins and phthalocyanines, and corrode with four nitrogen atoms, which form coordination sites with stabilized TM-N_4 compounds, enhancing their ORR catalytic activity. One of the most attractive features for macrocyclic compounds is that their electronic and catalytic properties can be improved by rationally designing and adjusting their ligand characters. Metal macrocycles, such as porphyrins and phthalocyanines doped with TMs (Fe, Co or Ni), are one of the most widely used precursors for preparing ORR electrocatalysts. In 1964, Jasinski first observed that metal macrocycles could promote the ORR of fuel cells and conducted in-depth research on them as potential cathode catalysts in metal-air flow batteries [zinc-air flow batteries (ZAFBs)] and fuel cells[25]; the researchers found that metal atom occupies the center of the macrocycle cavity with maximum stability, which radically facilitates the catalytic activity of ORR electrocatalysts[26-31]. In addition, high ORR catalytic activity was found existing in macrocyclic containing TM-N_4 centers (especially CoN_4 or FeN_4 moiety), such as porphyrins compounds (tetramethoxyphenyl-porphyrin, tetraphenyl-porphyrin, phthalocyanine compounds, and tetraazanthracene)[32,33]. Therefore, metal macrocycle-based catalysts have been extensively studied from synthetic routes to electrocatalytic mechanisms, especially for Fe-based or Co-based porphyrins[34]. However, relatively poor intrinsic conductivity of metallomacrocycles affects the electron transport during electrocatalysis and leads to their behindhand electrocatalytic performance.

The high-temperature pyrolysis for preparing carbon-based catalysts is crucial to improving the ORR catalytic activity of metal macrocyclic systems. The preparation of TM-doped nitrogen-carbon-based catalysts through carbonization of metallophthalocyanine/porphyrin macrocycles has been extensively studied in the field of electrocatalytic materials, and significant progress has been made in terms of oxygen reduction reactivity and lifetime[35]. For example, Choi *et al*. realized the direct construction of an ordered mesoporous three-dimensional iron-porphyrin catalyst by pyrolyzing the FeN_4 complex (tetrapyridyl porphyrin iron) and SBA-15[36]. Compared with Fe-N-C catalysts prepared by carbonizing various precursors on carbon supports, porphyrin-like iron materials completely avoid the addition of additional carbon supports, and the Fe-N_x active sites are uniformly distributed in mesoporous graphite matrix with high specific surface areas. These structures effectively increase the density of effective catalytic sites and promote the transport property of oxygen in macropores and mesopores, accelerating the kinetic of ORR. These characteristics make them an excellent ORR catalytic material.

Recently, a series of new porous materials with covalently linked periodic frameworks and conjugated structures, i.e., macrocycle-based covalent organic polymers (COPs), have been developed[37-40]. They are equipped with superior tailorability in functional design and structure regulation[41-43], so that after pyrolysis, the riveting positions of doped heteroatoms and metal sites in COP precursors can be well predesigned[44]. For example, in recent studies, our group used the Yamamoto coupling reaction to controllably synthesize two-dimensional macrocycle-based COPs with quasi-phthalocyanine structures coordinating with Ni, Fe and Co metal ions and prepared non-noble metal-doped ORR catalysts by high-temperature pyrolysis towards COP precursors[45,46]. Due to the inherent rigid structural characteristics and flexible, adjustable structural design similar to the covalent organic framework (COF)[29], the predesigned catalytic site structure

can be maintained to some extent during the high-temperature pyrolysis process, which guarantees the ideal ORR catalytic activity compared with the direct calcination towards carbon, nitrogen and metal-containing composites. Under alkaline conditions, the ORR catalytic activity of COP-based NPMCs achieved great performance improvement. Compared with Pt/C, the Co-doped catalyst showed a higher limiting current density, and its kinetic current is 1.4 times that of the Pt/C catalyst.

Inspired by the above studies, here, we utilized the molecular model of macrocyclic COP to design and prepare nitrogen-coordinated precursor structures and obtained COP_{MCT}-Co-900 electrocatalysts with excellent oxygen reduction activity through subsequent high-temperature carbonization. We extended this strategy to two other COPs with different macrocycle structures and studied the effects of precursors, metal sources and carbonization temperature on the oxygen reduction performance of catalysts. The results show that the COP_{MCT}-Co-900 catalyst exhibits the best oxygen reduction performance, and the half-wave potential ($E_{1/2}$) reached 0.85 V [*vs.* reversible hydrogen electrode (RHE)] under alkaline test conditions, which is comparable to commercial Pt/C. After 50,000 s of chronoperometric testing, the current density of COP_{MCT}-Co-900 decreased by 3.2% (*vs.* Pt/C decreased by 21.9%), indicating their stable durability. In addition, the self-made rechargeable ZAFB using COP_{MCT}-Co-900 catalyst as the air cathode showed a superior power density (155.6 $mW \cdot cm^{-2}$) and superior cycle life (90 h, 270 cycles). The preparation strategy points out a new direction for high-performance oxygen electrodes.

EXPERIMENTAL SECTION

Chemicals

Ferric nitrate hexahydrate (99%) (Alfa Aesar), Cobal nitrate hexahydrate (99+%) (ACROS Organics), Nickel nitrate hexahydrate (Alfa Aesar), benzene-1,2,4,5-tetracarbonitrile (BTC) (99%) (Bide Medical), 3,5-diamino-1,2,4-triazole (DTZ) (Sigma Andrich), 2,6-diaminopyridine (DPD), 1,3,4thiadiazole-2,5-diamine (TZD), methanol (99.8+%) (Fisher Chemical), and isopropanol (Fisher Chemical), 5.0 wt% Nafion (Du Pont), 20% Pt/C (JM).

Preparation of COP_{MCT}-M

DTZ was employed as monomers to polymerize with BTC and generated the corresponding products, denoted as COP_{MCT}-Co, respectively. Typically, BTC and corresponding monomers were added to 60 mL ethylene glycol under the molar ratio of 1:2.4, and then ultrasound for 5 min to obtain solution A. Additionally, 1.2 equivalent amounts of metal salt, such as iron, cobalt, and nickel salts, were added to 20 mL ethylene glycol, and homogenized solution B was obtained by ultrasound. Solution B was rapidly introduced into solution A, and the microwave reactor was used to react at 180 °C for 1 h. After centrifugation, washing with ethylene glycol, ethanol and water four times, dry overnight in a vacuum drying oven at 70 °C.

Preparation of COP_{MCT}-M-900

COP_{MCT}-M is ground into a powder, carbonized in a tube furnace for 2 h (900 °C), and naturally cooled to obtain COP_{MCT}-M-900.

Physical characterization

The microstructure of the samples was obtained by scanning electron microscope (TESCAN, MAIA 3 XMU) and transmission electron microscope (Hitachi, HT7700). X-ray diffractometer (XRD) data were measured by XRD-7000. Sample compositions were measured by X-ray photoelectron spectroscopy (XPS) (Thermo Fischer, ESCALAB). The Fourier transform infrared spectroscopy (FT-IR) analysis was performed on a Nicolet 8700/Continuum XL. The valence structure of the sample was measured by an X-ray photoelectron spectrometer (THERMO VG, ESCALAB 250). The molecular structure information was

obtained by a Raman spectrometer (HORIBA JOBIN YVON SAS, LabRAM HR Evolution), and the specific surface area and pore distribution were determined by BET-ASAP2460.

Electrochemical measurements

We used the CHI electrochemical instrument to perform electrochemical tests on the samples through a three-electrode system, in which the working electrode was coated with a glassy carbon electrode of the sample to be tested. Saturated calomel and graphite rod were used as the reference and counter electrodes, respectively. Furthermore, 5 mg catalyst is evenly dispersed in the mixed solution of ethanol (950 μL) and 5% Nafion (50 μL) by ultrasound, and the ink is coated on the surface of the glass carbon electrode. The working electrode with a load of 0.76 mg·cm^{-2} was obtained by natural drying (the load of Pt/C was 0.25 mg·cm^{-2}). The hydrogen peroxide yield and the electron transfer number were obtained by rotating ring disk electrode (RRDE) and calculated according to the following Equations (1) and (2):

$$n = \frac{4I_d}{N(I_d + I_r/N)} \quad (1)$$

$$HO_2^-(\%) = \frac{200I_r}{N(I_d + I_r/N)} \quad (2)$$

Kouteckye-Levich (K-L) Equations (3)-(5):

$$\frac{1}{J} = \frac{1}{J_l} + \frac{1}{J_k} = \frac{1}{J_k} + \frac{1}{B\omega^{1/2}} \quad (3)$$

$$B = 0.62nFC_0D_0^{2/3}v^{-1/6} \quad (4)$$

$$J_k = \frac{J \times J_i}{J_L - J} \quad (5)$$

Where I_r, I_d, J, N, J_k, B, J_L, ω, n, F, C_0, ν, and D_0 represent respectively the ring current, the disk current, the measured current density, the ring collection efficiency, the angular velocity of the electrode (rpm), the reciprocal slope of equation, the transferred electron number, the kinematic viscosity of the electrolyte, the kinetic and diffusion-limiting current density, the Faraday constant, the bulk concentration of O_2, (1.93×10^{-5} cm^2·s^{-1}), and the O_2 diffusion coefficient. The electrochemically active surface area of the sample was calculated using the following Equation (6):

$$ECSA = \frac{j/v}{C_{GC}} \quad (6)$$

where *v*: scan rate, C_{GC}: double layer capacitance, j: measured current density.

Recharge ZAFBs assembly

The test steps of the rechargeable ZAFBs are as follows: (1) The electrolyte is configured. In addition, 6 M KOH and 0.2 M ZnO are dissolved in deionized water; (2) The air cathode is prepared and the sample is configured into a uniform ink and sprayed on carbon paper with a gas diffusion layer, and the sample load is 2mg·cm^{-2}; (3) Anode preparation, polishing of 0.3 mm thick zinc sheet; (4) The above materials are assembled into ZAFBs, and the electrolyte flow rate is set at 5mL·min^{-1}.

RESULTS AND DISCUSSION

As shown in Scheme 1, we utilize BTC and DTZ with high symmetric functionalities as reaction monomers to polycondense into chain hemiporphyrocyanogen COP rich in CoN_4 active centers, denoted as COP_{MCT}-Co. Subsequently, the COP_{MCT}-Co-900 catalyst was obtained by pyrolysis of COP_{MCT}-Co precursor at high-temperature conditions of 900 °C.

The structural information of the COP_{MCT}-Co precursor was confirmed by solid-state ^{13}C nuclear magnetic resonance spectroscopy (NMR) [Figure 1A]. The characteristic peak at (a) 160.73 ppm is attributed to the carbon moiety on the five-membered ring connecting the nitrogen atom in the benzpyrole. The characteristic peak at (b) 153.7 ppm is ascribed to the carbon-containing moiety in the DTZ monomer; the characteristic peaks at (c) 140.74, (d) 126.0, (e) 115.47 ppm were attributed to the carbon atom of the benzene ring in the indole ring, respectively. We conducted high-resolution transmission electron microscopy (HRTEM) tests on the catalyst to further determine its composition and structure [Figure 1B and C]. The obvious cobalt nanoparticles were observed in Figure 1B. After further local magnification, we find that obvious lattice fringes with a lattice spacing of 0.20 nm [corresponding to the (111) crystal plane of cobalt nanoparticles] and 0.34 nm [corresponding to the (002) crystal plane of carbon matrix], respectively, indicating that Co-N-C catalyst loaded with Co nanoparticles has been successfully synthesized. Then, the elemental composition and chemical states of the COP_{MCT}-Co-900 were tested by XPS [Figure 1D-F and Supplementary Figure 1]. COP_{MCT}-Co is mainly composed of Co, N, O and C elements, of which C occupies the highest content, reaching 67.85%, followed by N, O and Co elements, accounting for 16.47%, 14.7% and 0.98%, respectively. The high-resolution Co 2p XPS spectra of COP_{MCT}-Co-900 are deconvoluted into Co $2p_{3/2}$, Co $2p_{1/2}$, and Co-N_4 moieties and other satellites. The high-resolution N 1s XPS spectra of COP_{MCT}-Co-900 are deconvoluted into graphitic N (401.2 eV), pyrrolic N (398.8 eV), and Co-N_x (399.8 eV) moieties[47]. The high-resolution C 1s XPS spectra of COP_{MCT}-Co-900 are deconvoluted into C-N, C=C, C=O, and C-O moieties. These results indicate that in the COP_{MCT}-Co-900 catalyst, in addition to cobalt nanoparticles, another part of the Co atom is present in the COP_{MCT}-Co-900 catalyst in the form of an active moiety of CoN_x.

We performed FT-IR tests on BTC and our as-synthesized COP_{MCT}-Co polymer [Figure 2A]. The monomer BTC exhibits a strong characteristic peak at 2,245 cm^{-1}, corresponding to the stretching vibration peak of -C≡N. However, the COP_{MCT}-Co polymer showed almost no characteristic peak at 2,245 cm^{-1}, indicating that BTC and DTZ monomers have been successfully polymerized. Besides, the COP_{MCT}-Co exhibits the characteristic peaks at 1,646 and 1,536 cm^{-1}, which are attributed to -C=N moiety and conjugate rings, respectively. These results indicate that BTC monomers reacted with DTZ and cobalt atoms to form COP_{MCT}-Co. Further, we analyzed the specific surface area and pore distribution of COP_{MCT}-Co-900 catalyst. The pore distribution shows that the COP_{MCT}-Co-900 catalyst is dominated by mesoporous pores and contains a certain amount of macropores [Figure 2B]. This pore structure facilitates the diffusion of active substances and reduces the resistance to mass transfer. Figure 2C shows that the COP_{MCT}-Co-900 has a large specific surface area (288.5 $m^2 \cdot g^{-1}$), facilitating full exposure with the active site. The catalyst was characterized by Raman spectra to investigate the graphitization degree of the COP_{MCT}-Co-900 sample [Figure 2D]. Figure 2D shows that the I_D/I_G value of COP_{MCT}-Co-900 is 0.92, indicating that the catalyst keeps a higher graphitization degree and conductivity, which is also confirmed by the HRTEM image in Figure 1C. We further performed the XRD spectra to analyze the chemical composition and crystal structure of COP_{MCT}-Co and COP_{MCT}-Co-900 [Figure 2E and F]. We found that this material has only a wide peak, which indicates that COP_{MCT}-Co precursor exists in an amorphous form. Figure 2F shows the XRD pattern after carbonization. It can be seen from the Figure 2F that COP_{MCT}-Co-900 has diffraction peaks at 26.31°, 44.2°, 51.5° and 75.9°. The diffraction peak at 26.31° corresponds to the (002) crystal face of carbon.

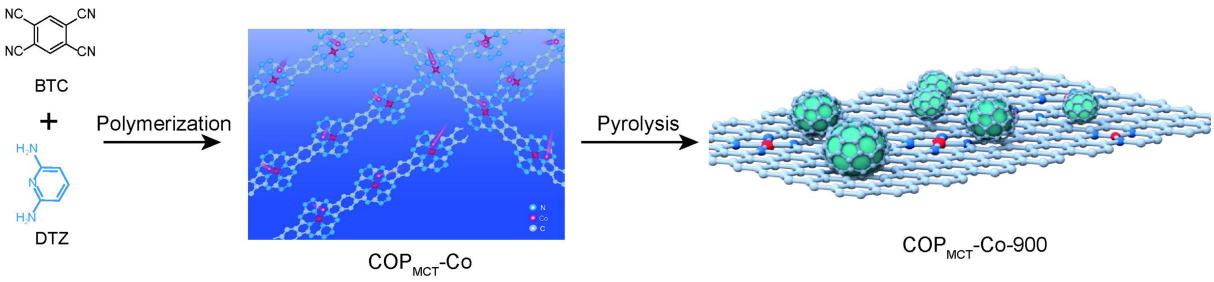

Scheme 1. Schematic diagram of the synthesis of COP$_{MCT}$-Co-900 catalyst. COP: Covalent organic polymer.

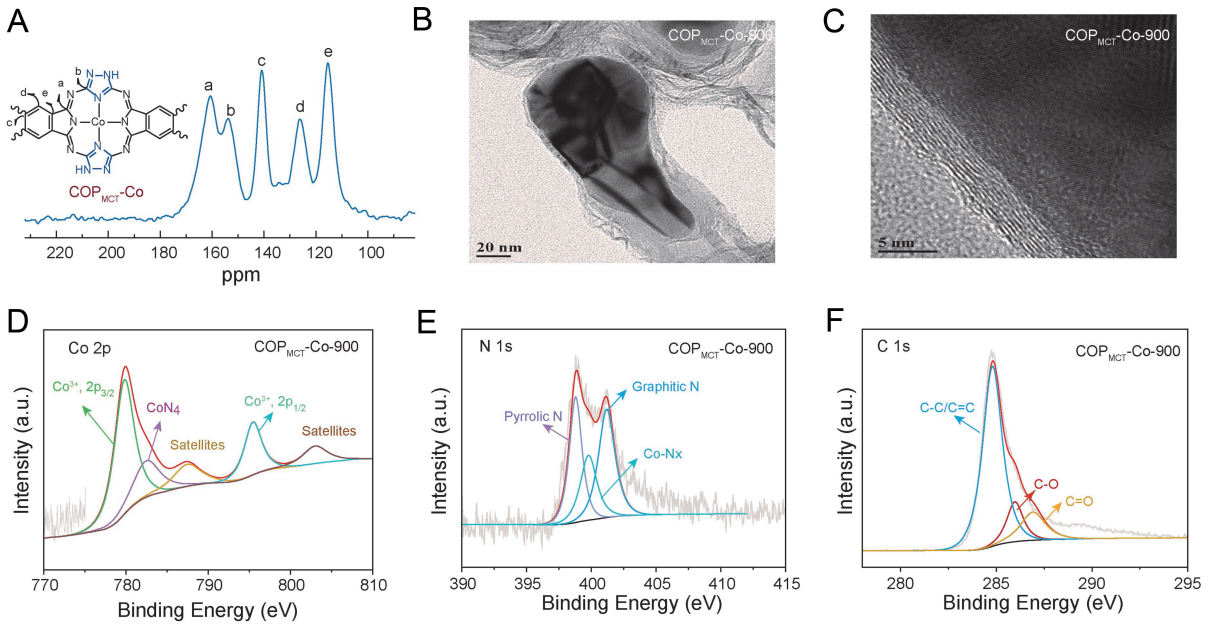

Figure 1. (A) NMR spectra of COP$_{MCT}$-Co; (B and C) HRTEM images of COP$_{MCT}$-Co-900 at different scales; (D) High-resolution Co 2p XPS for COP$_{MCT}$-Co-900; (E) High-resolution N 1s XPS for COP$_{MCT}$-Co-900; (F) High-resolution C 1s XPS for COP$_{MCT}$-Co-900. NMR: Nuclear magnetic resonance spectroscopy; COP: covalent organic polymer; HRTEM: high-resolution transmission electron microscopy; XPS: X-ray photoelectron spectroscopy.

The diffraction peaks of 44.3°, 53.5° and 76.9° correspond to the (111), (200) and (220) crystal faces of cobalt nanoparticles, respectively, proving the existence of cobalt nanoparticles in COP$_{MCT}$-Co-900.

We conducted electrochemical tests on COP$_{MCT}$-Co at different carbonized temperatures to explore the effect of carbonization temperature on catalyst performance. Figure 3A shows the oxygen reduction polarization curves of catalysts carbonized at 800-1,000 °C. The results show that the oxygen reduction performance of the catalyst obtained by carbonization at 900 °C is optimal. The COP$_{MCT}$-Co-900 has the best electrochemical performance, with an initial potential of 0.97 V, a limited current density of 6.1 mA·cm^{-2}, and a $E_{1/2}$ of 0.85 V. Figure 3B shows the $E_{1/2}$ of the catalyst at these five carbonization temperatures. In the range of 800~1000 °C, the $E_{1/2}$ of the catalyst first increases and then decreases with rising temperature, indicating 900 °C as the optimal carbonization temperature. Having fast oxygen reduction kinetics is very important for the catalyst performance index. As shown in Figure 3C, the oxygen reduction polarization

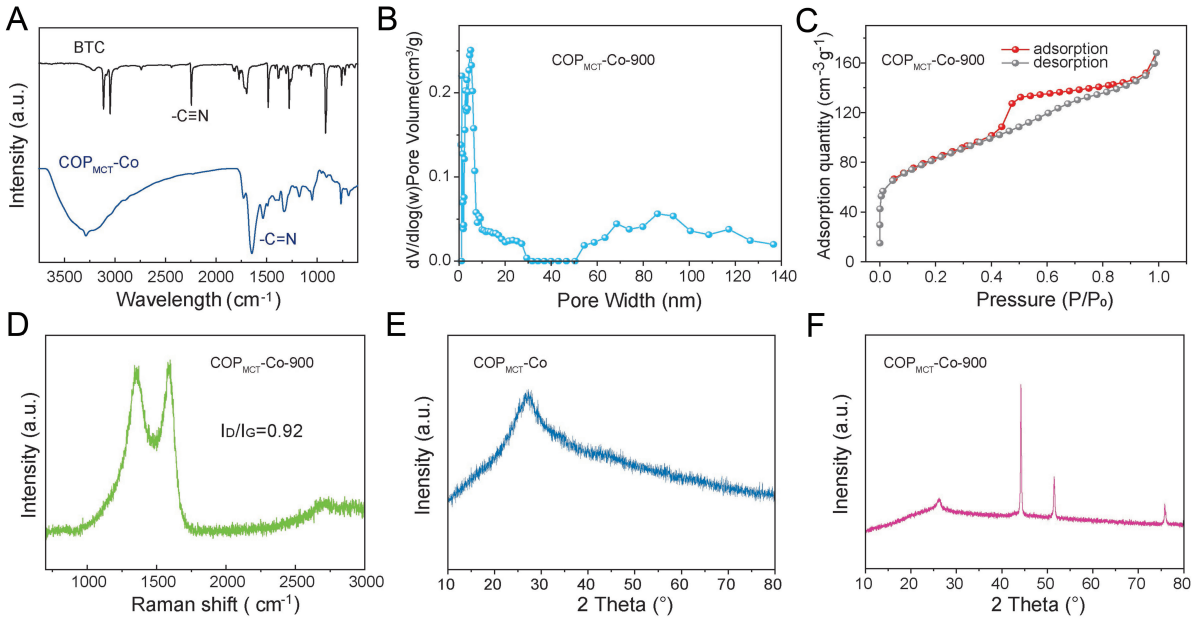

Figure 2. (A) FT-IR spectra of BTC and COP$_{MCT}$-Co; (B) The corresponding pore distribution of COP$_{MCT}$-Co-900; (C) N_2 adsorption and desorption isotherm of COP$_{MCT}$-Co-900; (D) Raman spectra of COP$_{MCT}$-Co-900; XRD spectra of (E) COP$_{MCT}$-Co and (F) COP$_{MCT}$-Co-900. FT-IR: Fourier transform infrared spectroscopy; BTC: Benzene-1,2,4,5-tetracarbonitrile; COP: covalent organic polymer; XRD: X-ray diffractometer.

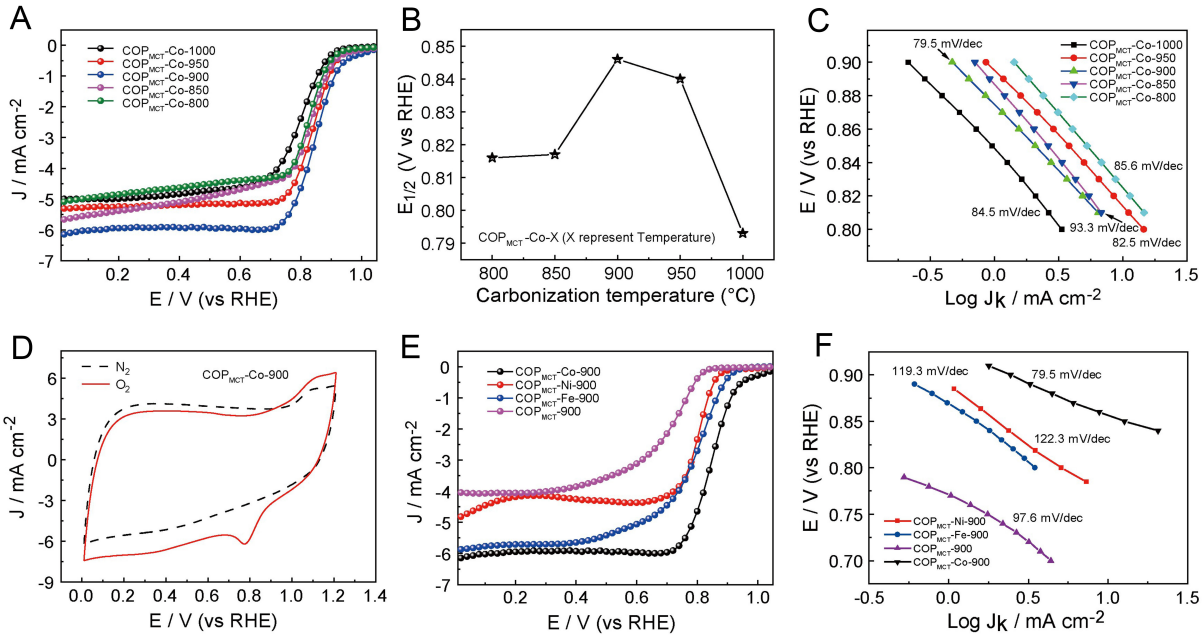

Figure 3. (A) The LSV curves of COP$_{MCT}$-Co-X (X represent pyrolysis temperature) catalysts at different temperatures; (B) $E_{1/2}$ of COP$_{MCT}$-Co-X catalysts at different temperatures; (C) Tafel plots of COP$_{MCT}$-Co-X; (D) The CV curves of COP$_{MCT}$-Co-900; (E) The LSV curves of COP$_{MCT}$-Co-900, COP$_{MCT}$-Ni-900, COP$_{MCT}$- 900 and COP$_{MCT}$-Fe-900; (F) Tafel plots of COP$_{MCT}$-Co-900, COP$_{MCT}$-Ni-900, COP$_{MCT}$- 900 and COP$_{MCT}$-Fe-900. LSV: Linear sweep voltammetry; COP: covalent organic polymer; CV: cyclic voltammetry.

curves of catalysts carbonized at various carbonization temperatures were converted into the Tafel slope. The COP$_{MCT}$-Co-900 delivers a Tafel slope of 79.5 mV·dec^{-1}. Therefore, COP$_{MCT}$-Co-900 maintains the best

oxygen reduction kinetics, and 900 °C is the optimal temperature for catalyst carbonization. We first performed cyclic voltammetry (CV) tests on the catalyst in an alkaline electrolyte (0.1 M KOH aqueous solution) [Figure 3D]. An obvious oxygen reduction peak for the catalyst appears at ~0.8 V (*vs.* RHE). By contrast, we tested its CV test in nitrogen-saturated 0.1 mol·L^{-1} KOH solution, and no peak appears in the range of 0-1.2 V (*vs.* RHE), indicating the superior ORR catalytic activity of COP_{MCT}-Co-900. In addition, we explored the effects of diverse doping metals on oxygen reduction activity and synthesized COP_{MCT}-Co-900, COP_{MCT}-Ni-900, COP_{MCT}-900, and COP_{MCT}-Fe-900. The results showed that COP_{MCT}-Co-900 maintains the best ORR activity and ORR kinetics compared to COP_{MCT}-900 catalysts with other metal centers [Figure 3E and F].

In order to prove the universality and versatility of the method, we have successfully prepared two other Co-based chain COP precursors using DPD and TDZ monomers, denoted as COP_{MCT}-Co, COP_{MCP}-Co and COP_{MCZ}-Co [Supplementary Figure 2]. Linear sweep voltammetry (LSV) curve results show that the ORR catalytic performance of COP_{MCT}-Co is the highest compared with other catalysts. Through quantitative calculation analysis of the precursor, we found that the electrostatic potential of COP_{MCT}-Co is between COP_{MCZ}-Co and COP_{MCZ}-Co, and the adsorption strength of oxygen intermediates is moderate, which is conducive to both the oxygen adsorption process and the oxygen desorption process. Therefore, COP_{MCT}-Co shows excellent ORR performance [Supplementary Figure 3]. After high-temperature pyrolysis of 900 °C towards COP_{MCP}-Co and COP_{MCZ}-Co precursors, the COP_{MCP}-Co-900 and COP_{MCT}-Co-900 catalysts were obtained, respectively. We evaluated their catalytic activity through LSV curves [Figure 4A]. All catalysts have demonstrated satisfactory ORR catalytic activity. Among them, COP_{MCT}-Co-900 exhibits the highest catalytic activity, and its $E_{1/2}$ reaches 847 V; COP_{MCP}-Co-900 maintains the second highest catalytic activity, and its $E_{1/2}$ reaches 798 V; the $E_{1/2}$ of COP_{MCT}-Co-900 is approximately 751 V. We continue to test the LSV curves of the samples at varying rotational speeds to further explore the catalytic process of the catalyst. Based on these curves, K-L equations at different voltages were derived. As shown in Figure 4B, the current increases proportionally as the rotation speed increases. Figure 4C exhibits the K-L equation based on the oxygen reduction polarization curve in Figure 4B. The number of electron transfers can be further obtained by fitting the slope of the curve of the K-L equation. According to the data, the electron transfer number of COP_{MCT}-Co-900 is close to 4, indicating that COP_{MCT}-Co-900 maintains a high selectivity for the ORR process. Good cycle stability is the basis of the commercial application of catalysts. We compared the stability of COP_{MCT}-Co-900 with that of commercial Pt/C by a potentiostatic method. As can be seen from Figure 4D, after 50,000 s of chronoamperometry testing, the current density of COP_{MCT}-Co-900 decreased by 3.2%, while the current density loss of Pt/C is more than 21.9%. Further, we evaluated the electron transfer number (N_e) and hydrogen peroxide yield of the catalyst ORR by RRDE [Figures 4E and F]. In the range of 0.2-0.8 V, the hydrogen peroxide yield of COP_{MCT}-Co, COP_{MCT}-Co-900 and the Pt/C reach 67%-93%, 1.4%-4.4% and 1.6%-3.6%, respectively. The low hydrogen peroxide yield proves the high selectivity for four-electron ORR. The N_e of COP_{MCT}-Co is close to 2.5, while that of COP_{MCT}-Co-900 and Pt/C is close to 4, which indicates that COP_{MCT}-Co-900 and Pt/C follow a four-electron reaction.

Furthermore, we evaluated the performance of COP_{MCT}-Co-900 in energy conversion devices ZAFBs, fabricated COP_{MCT}-Co-900 as an air cathode catalyst of ZAFBs, and investigated its performance in ZAFBs [Figure 5A]. When COP_{MCT}-Co-900 was used as the cathode catalyst for ZAFBs, the power density of 155.6 mW·cm^{-2} was significantly higher than that of the Pt/C catalyst (101.7 mW·cm^{-2}) under the same test conditions [Figure 5B]. This result can be explained by the discharge polarization curves of the two, which show that the voltage of COP_{MCT}-Co-900 drops more slowly as the current density increases. The polarization curve of COP_{MCT}-Co-900 declines more slowly than that of Pt/C, indicating a lower internal

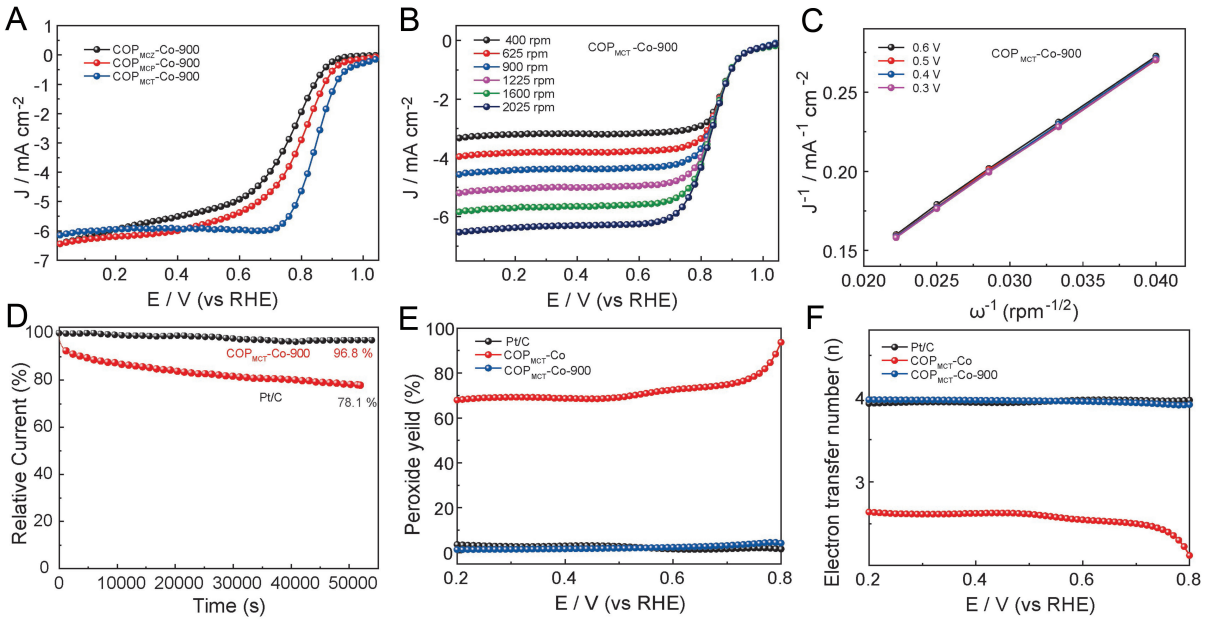

Figure 4. (A) ORR LSV curves of COP$_{MCT}$-Co-900, COP$_{MCP}$-Co-900 and COP$_{MCZ}$-Co-900; (B) LSV of COP$_{MCT}$-Co-900 at different rotating rates; (C) The corresponding K-L plots at various potentials, respectively; (D) I-t curves performed of COP$_{MCT}$-Co-900 and Pt/C; (E) Hydrogen peroxide yield of COP$_{MCT}$-Co, COP$_{MCT}$-Co-900 and Pt/C; (F) Electron transfer numbers of COP$_{MCT}$-Co, COP$_{MCT}$-Co-900 and Pt/C. ORR: Oxygen reduction reaction; LSV: linear sweep voltammetry; COP: covalent organic polymer.

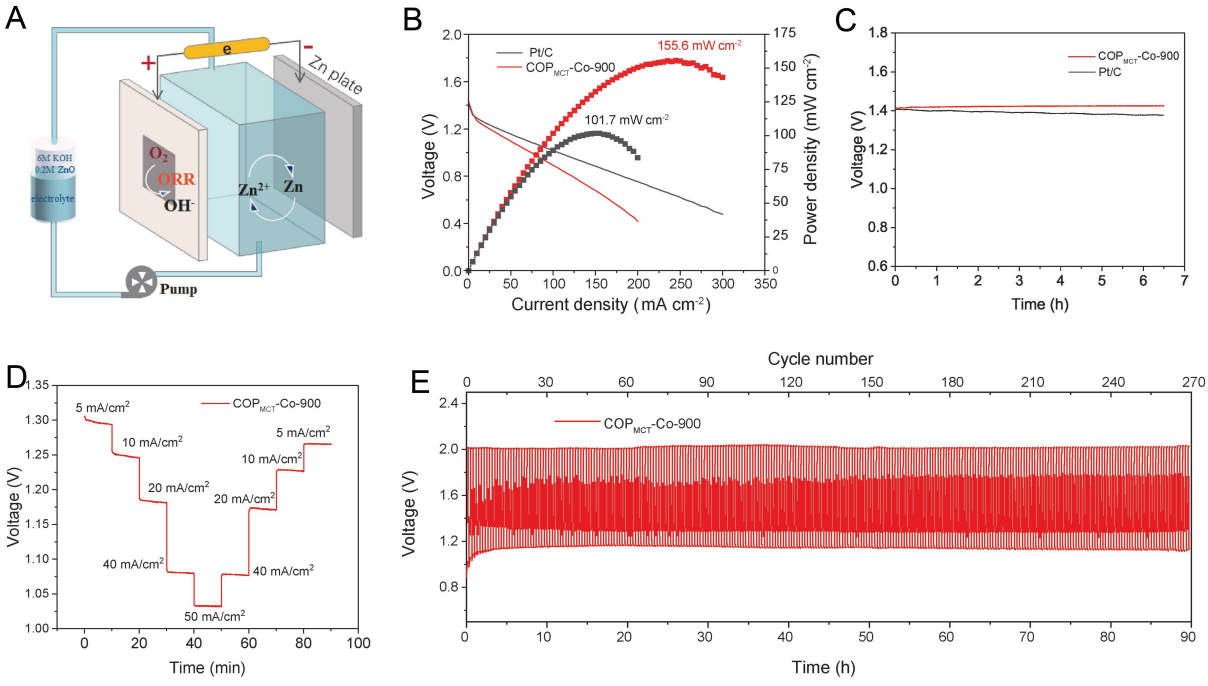

Figure 5. (A) A schematic configuration of the homemade Zn-air battery; (B) Comparison of polarization and power density curves using Pt/C and COP$_{MCT}$-Co-900 as catalysts; (C) Open circuit plot of the Zn-air battery using COP$_{MCT}$-Co-900 and Pt/C as catalysts; (D) Cycle discharge curves of COP$_{MCT}$-Co-900-driven Zn-air batteries at periodically changed current density; (E) Discharge/charge cycling performance of Zn-air batteries with COP$_{MCT}$-Co-900 as catalyst at a current density of 10 mA·cm^{-2}. COP: Covalent organic polymer.

resistance. Figure 5C shows that ZAFBs assembled with the COP_{MCT}-Co-900 maintain a high open circuit voltage of around 1.43 V for a long time, which is superior to the Pt/C catalyst, demonstrating a lower impedance in the COP_{MCT}-Co-900-powered ZAFBs. Notably, at current densities of 5, 10, 20, 40, or even 50 $mA·cm^{-2}$, sustained discharge performance measurements show only slight attenuation for ZAFBs assembled with COP_{MCT}-Co-900 catalyst after successive alternating cycles [Figure 5D]. We then tested the cyclic stability of ZAFBs by setting a constant charge and discharge current. The cycle life of the ZAFBs based on COP_{MCT}-Co-900 exceeds 90 h, demonstrating its excellent charge-discharge performance and great application potential [Figure 5E].

CONCLUSION

In conclusion, we demonstrate a rational design method for preparing ORR electrocatalysts with the assistance of a predesigned macrocyclic COP model molecular. Three kinds of metal macrocyclic COP materials with metal-N_4 structures were prepared by a simple microwave-assisted method. The non-precious metal N/C electrocatalyst was obtained by carbonizing the metal macrocyclic COP precursor at high temperatures. Thanks to the high electrical conductivity, uniformly dispersed active sites and excellent robustness of the substrate, the synthesized COP_{MCT}-Co-900 has excellent ORR performance, long lifetime and high tolerance to methanol. The $E_{1/2}$ reaches 0.85 V (*vs.* RHE) under alkaline test conditions, and the current density of the catalyst only decreased by 3.2% after 50,000 s of chronoamperometry testing. In addition, COP_{MCT}-Co-900 exhibited excellent power density (155.6 $mW·cm^{-2}$) and exceptional stability (90 h) when used as a cathode catalyst in ZAFBs. This study not only provides a promising non-valuable ORR electrocatalyst to replace Pt but also points out a new direction for developing high-performance oxygen electrodes.

DECLARATIONS

Authors' contributions

Performed the synthesis, structural characterizations and electrochemical tests: Li X
Made substantial contributions to the conception and design of the study, performed data analysis and interpretation, and wrote the original draft: Leng Y
Supervised and led this project and revised the manuscript repeatedly: Xiang Z, Li X
Performed partial electrochemical tests and ZAFB device assembly: Chen T, Yin Y, Li J
All authors provided critical feedback and helped shape the research and paper. All authors commented on the paper.

Availability of data and materials

Not applicable.

Financial support and sponsorship

This work was supported by the National Key Research and Development Program of China (2022YFB3807500); the NSF of China (22220102003); the Beijing Natural Science Foundation (JL23003); "Double-First-Class" construction projects (XK180301, XK1804-02); China Postdoctoral Science Foundation (2023TQ0020) and Postdoctoral Fellowship Program of CPSF (GZC20230199).

Conflicts of interest

All authors declared that there are no conflicts of interest.

Ethical approval and consent to participate

Not applicable.

Consent for publication

Not applicable.

REFERENCES

1. King LA, Hubert MA, Capuano C, et al. A non-precious metal hydrogen catalyst in a commercial polymer electrolyte membrane electrolyser. *Nat Nanotechnol* 2019;14:1071-4. DOI
2. Varnell JA, Tse EC, Schulz CE, et al. Identification of carbon-encapsulated iron nanoparticles as active species in non-precious metal oxygen reduction catalysts. *Nat Commun* 2016;7:12582. DOI PubMed PMC
3. Malko D, Kucernak A, Lopes T. *In situ* electrochemical quantification of active sites in Fe-N/C non-precious metal catalysts. *Nat Commun* 2016;7:13285. DOI PubMed PMC
4. Bashyam R, Zelenay P. A class of non-precious metal composite catalysts for fuel cells. *Nature* 2006;443:63-6. DOI PubMed
5. Leng Y, Yang B, Zhao Y, Xiang Z. Fluorinated bimetallic nanoparticles decorated carbon nanofibers as highly active and durable oxygen electrocatalyst for fuel cells. *J Energy Chem* 2022;73:549-55. DOI
6. Li X, Liu Q, Yang B, Liao Z, Yan W, Xiang Z. An initial covalent organic polymer with closed-F edges directly for proton-exchange-membrane fuel cells. *Adv Mater* 2022;34:e2204570. DOI PubMed
7. Bates JS, Johnson MR, Khamespanah F, Root TW, Stahl SS. Heterogeneous M-N-C catalysts for aerobic oxidation reactions: lessons from oxygen reduction electrocatalysts. *Chem Rev* 2023;123:6233-56. DOI PubMed PMC
8. Liu J, Wan X, Liu S, et al. Hydrogen passivation of M-N-C (M = Fe, Co) catalysts for storage stability and ORR activity improvements. *Adv Mater* 2021;33:2170300. DOI
9. Patniboon T, Hansen HA. Acid-stable and active M-N-C catalysts for the oxygen reduction reaction: the role of local structure. *ACS Catal* 2021;11:13102-18. DOI
10. Shi Q, He Y, Bai X, et al. Methanol tolerance of atomically dispersed single metal site catalysts: mechanistic understanding and high-performance direct methanol fuel cells. *Energy Environ Sci* 2020;13:3544-55. DOI
11. Sun K, Dong J, Sun H, et al. Co(CN)3 catalysts with well-defined coordination structure for the oxygen reduction reaction. *Nat Catal* 2023;6:1164-73. DOI
12. Sun Y, Silvioli L, Sahraie NR, et al. Activity-selectivity trends in the electrochemical production of hydrogen peroxide over single-site metal-nitrogen-carbon catalysts. *J Am Chem Soc* 2019;141:12372-81. DOI PubMed
13. Zhao CX, Li BQ, Liu JN, Zhang Q. Intrinsic electrocatalytic activity regulation of M-N-C single-atom catalysts for the oxygen reduction reaction. *Angew Chem Int Ed Engl* 2021;60:4448-63. DOI PubMed
14. Singh SK, Kashyap V, Manna N, et al. Efficient and durable oxygen reduction electrocatalyst based on CoMn alloy oxide nanoparticles supported over N-doped porous graphene. *ACS Catal* 2017;7:6700-10. DOI
15. Chen Z, Higgins D, Yu A, Zhang L, Zhang J. A review on non-precious metal electrocatalysts for PEM fuel cells. *Energy Environ Sci* 2011;4:3167-92. DOI
16. Ratso S, Kruusenberg I, Käärik M, et al. Highly efficient transition metal and nitrogen co-doped carbide-derived carbon electrocatalysts for anion exchange membrane fuel cells. *J Power Sources* 2018;375:233-43. DOI
17. Yu Y, Zhou J, Sun Z. Novel 2D transition-metal carbides: ultrahigh performance electrocatalysts for overall water splitting and oxygen reduction. *Adv Funct Mater* 2020;30:2000570. DOI
18. Das TK, Jesionek M, Çelik Y, Poater A. Catalytic polymer nanocomposites for environmental remediation of wastewater. *Sci Total Environ* 2023;901:165772. DOI PubMed
19. Feng X, Bai Y, Liu M, et al. Untangling the respective effects of heteroatom-doped carbon materials in batteries, supercapacitors and the ORR to design high performance materials. *Energy Environ Sci* 2021;14:2036-89. DOI
20. Cheon JY, Kim JH, Kim JH, Goddeti KC, Park JY, Joo SH. Intrinsic relationship between enhanced oxygen reduction reaction activity and nanoscale work function of doped carbons. *J Am Chem Soc* 2014;136:8875-8. DOI PubMed
21. Liu M, Sun T, Peng T, et al. Fe-NC single-atom catalyst with hierarchical porous structure and P−O bond coordination for oxygen reduction. *ACS Energy Lett* 2023;8:4531-9. DOI
22. Wang Y, Li K, Cheng R, et al. Enhanced electronic interaction between iron phthalocyanine and cobalt single atoms promoting oxygen reduction in alkaline and neutral aluminum-air batteries. *Chem Eng J* 2022;450:138213. DOI
23. Madhavachary R, Abdelraheem EMM, Rossetti A, et al. Two-step synthesis of complex artificial macrocyclic compounds. *Angew Chem Int Ed Engl* 2017;56:10725-9. DOI PubMed PMC
24. Luo Y, Chen Y, Xue Y, et al. Electronic structure regulation of iron phthalocyanine induced by anchoring on heteroatom-doping carbon sphere for efficient oxygen reduction reaction and Al-Air battery. *Small* 2022;18:e2105594. DOI PubMed
25. Jasinski R. A new fuel cell cathode catalyst. *Nature* 1964;201:1212-3. DOI
26. Shao M, Chang Q, Dodelet JP, Chenitz R. Recent advances in electrocatalysts for oxygen reduction reaction. *Chem Rev* 2016;116:3594-657. DOI PubMed

27. Luo M, Zhao Z, Zhang Y, et al. PdMo bimetallene for oxygen reduction catalysis. *Nature* 2019;574:81-5. DOI
28. Wang HF, Chen L, Pang H, Kaskel S, Xu Q. MOF-derived electrocatalysts for oxygen reduction, oxygen evolution and hydrogen evolution reactions. *Chem Soc Rev* 2020;49:1414-48. DOI PubMed
29. Li X, Xiang Z. Identifying the impact of the covalent-bonded carbon matrix to FeN_4 sites for acidic oxygen reduction. *Nat Commun* 2022;13:57. DOI PubMed PMC
30. Li X, Liu D, Liu Q, Xiang Z. A pyrolysis-free method toward large-scale synthesis of ultra-highly efficient bifunctional oxygen electrocatalyst for zinc-air flow batteries. *Small* 2022;18:e2201197. DOI PubMed
31. Li X, Liu Y, Xiang Z. Dithiine bridged phthalocyanine-based covalent organic frameworks for highly efficient oxygen reduction reaction. *J Phys Chem C* 2022;126:4008-14. DOI
32. Yang S, Yu Y, Gao X, Zhang Z, Wang F. Recent advances in electrocatalysis with phthalocyanines. *Chem Soc Rev* 2021;50:12985-3011. DOI
33. Li X, Chen T, Yang B, Xiang Z. Fundamental understanding of electronic structure in FeN_4 site on electrocatalytic activity via dz^2-orbital-driven charge tuning for acidic oxygen reduction. *Angew Chem Int Ed Engl* 2023;62:e202215441. DOI PubMed
34. Liang Z, Guo H, Zhou G, et al. Metal-organic-framework-supported molecular electrocatalysis for the oxygen reduction reaction. *Angew Chem Int Ed Engl* 2021;60:8472-6. DOI
35. Wang X, Wang B, Zhong J, et al. Iron polyphthalocyanine sheathed multiwalled carbon nanotubes: a high-performance electrocatalyst for oxygen reduction reaction. *Nano Res* 2016;9:1497-506. DOI
36. Choi J, Kim J, Wagner P, et al. Highly ordered mesoporous carbon/iron porphyrin nanoreactor for the electrochemical reduction of CO_2. *J Mater Chem A* 2020;8:14966-74. DOI
37. Côté AP, Benin AI, Ockwig NW, O'Keeffe M, Matzger AJ, Yaghi OM. Porous, crystalline, covalent organic frameworks. *Science* 2005;310:1166-70. DOI PubMed
38. Liu Y, Diercks CS, Ma Y, et al. 3D covalent organic frameworks of interlocking 1D square ribbons. *J Am Chem Soc* 2019;141:677-83. DOI
39. Lyle SJ, Osborn Popp TM, Waller PJ, Pei X, Reimer JA, Yaghi OM. Multistep solid-state organic synthesis of carbamate-linked covalent organic frameworks. *J Am Chem Soc* 2019;141:11253-8. DOI PubMed
40. Lyu H, Diercks CS, Zhu C, Yaghi OM. Porous crystalline olefin-linked covalent organic frameworks. *J Am Chem Soc* 2019;141:6848-52. DOI PubMed
41. Diercks CS, Lin S, Kornienko N, et al. Reticular electronic tuning of porphyrin active sites in covalent organic frameworks for electrocatalytic carbon dioxide reduction. *J Am Chem Soc* 2018;140:1116-22. DOI
42. Nguyen HL, Hanikel N, Lyle SJ, Zhu C, Proserpio DM, Yaghi OM. A porous covalent organic framework with voided square grid topology for atmospheric water harvesting. *J Am Chem Soc* 2020;142:2218-21. DOI PubMed
43. Zhang B, Wei M, Mao H, et al. Crystalline dioxin-linked covalent organic frameworks from irreversible reactions. *J Am Chem Soc* 2018;140:12715-9. DOI
44. Gropp C, Ma T, Hanikel N, Yaghi OM. Design of higher valency in covalent organic frameworks. *Science* 2020;370:eabd6406. DOI PubMed
45. Yamamoto T, Hayashi Y, Yamamoto A. A novel type of polycondensation utilizing transition metal-catalyzed C-C coupling. I. preparation of thermostable polyphenylene type polymers. *Bull Chem Soc Jpn* 1978;51:2091-7. DOI
46. Zhou Z, Yamamoto T. Research on carbon - carbon coupling reactions of haloaromatic compounds mediated by zerovalent nickel complexes. Preparation of cyclic oligomers of thiophene and benzene and stable anthrylnickel(II) complexes. *J Organomet Chem* 1991;414:119-27. DOI
47. He Y, Guo H, Hwang S, et al. Single cobalt sites dispersed in hierarchically porous nanofiber networks for durable and high-power PGM-free cathodes in fuel cells. *Adv Mater* 2020;32:e2003577. DOI PubMed